



LAWRENCE
LIVERMORE
NATIONAL
LABORATORY

Three- and Two- Dimensional Simulations of Counter-propagating Shear Experiments at High Energy Densities at the National Ignition Facility

P. Wang, Y. Zhou, S. MacLaren, C. Hutington, K.
Raman, F. Doss, K. Flippo

September 3, 2015

Phys. Plasma

Disclaimer

This document was prepared as an account of work sponsored by an agency of the United States government. Neither the United States government nor Lawrence Livermore National Security, LLC, nor any of their employees makes any warranty, expressed or implied, or assumes any legal liability or responsibility for the accuracy, completeness, or usefulness of any information, apparatus, product, or process disclosed, or represents that its use would not infringe privately owned rights. Reference herein to any specific commercial product, process, or service by trade name, trademark, manufacturer, or otherwise does not necessarily constitute or imply its endorsement, recommendation, or favoring by the United States government or Lawrence Livermore National Security, LLC. The views and opinions of authors expressed herein do not necessarily state or reflect those of the United States government or Lawrence Livermore National Security, LLC, and shall not be used for advertising or product endorsement purposes.

Three- and Two- Dimensional Simulations of Counter-propagating Shear Experiments at High Energy Densities at the National Ignition Facility

Ping Wang, Ye Zhou, Stephan A. MacLaren, Channing M. Huntington, Kumar S. Raman

Lawrence Livermore National Laboratory, Livermore, California 94550

Forrest W. Doss, Kirk A. Flippo

Los Alamos National Laboratory, Los Alamos, New Mexico 87545

Abstract

Three- and two- dimensional numerical studies have been carried out to simulate recent counter-propagating shear flow experiments on the National Ignition Facility (NIF). A multi-physics three-dimensional, time-dependent radiation hydrodynamics simulation code is used. Using a Reynolds Averaging Navier-Stokes (RANS) model, we show that the evolution of the mixing layer width obtained from the simulations agrees well with that measured from the experiments. A sensitivity study is conducted to illustrate a 3D geometrical effect that could confuse the measurement at late times, if the energy drives from the two ends of the shock tube are asymmetric. Implications for future experiments are discussed.

1. Introduction

As pointed out by Phillips,¹ turbulence in nature is often the result of dynamical instability of shearing flows.² The Kelvin-Helmholtz (KH) instability³⁻⁴ is induced from an unstable perturbed interface between fluids subject to a parallel shear flow⁵ and is one of the classical problems in fluid dynamics. The development of KH instabilities often constitutes the critical step towards the onset of turbulent mixing observed both in the atmosphere and in oceans.⁶⁻⁷

Understanding the dynamics of the KH instability is important not only for its own sake, but also in the study of other hydrodynamic instabilities that one confronts in inertial confinement fusion (ICF) research.⁸ It has been established that the Rayleigh-Taylor (RT)⁹⁻¹⁰ and Richtmyer-Meshkov (RM)¹¹⁻¹² instabilities can cause the breaking of the capsule shells and prevent the ignition of the ICF devices¹³⁻¹⁶ by mixing the shell material into the fusion fuel.¹⁷ The KH instability is the reason for the evolution of the mushroom structures during the RT and RM nonlinear process,¹⁸⁻¹⁹ and it plays a critical role for the time-dependent transition to turbulence²⁰⁻²² of the flows driven by RT and RM instabilities.

In order to achieve the relevant ICF temperature and pressure regimes, several KH instability experiments have been performed at high energy density facilities. In the OMEGA experiments in Refs. [23-27], laser-driven shock waves propagated through low-density plastic foam placed on top of a higher-density plastic foil. Behind the shock front, lower-density foam plasma flowed over the higher-density plastic plasma. The interface between the foam and plastic was KH unstable. Other OMEGA experiments were carried out using the counterflowing geometries, in which the flows enter the apparatus from opposite directions.²⁸⁻³¹ This geometry was used to further increase the speed difference across the fluid interface. The designs of these laser experiments were based on traditional³²⁻³³ and counterflowing³⁴⁻³⁶ shear flow laboratory experiments performed in the liquid or gas phase.

The directly-laser-driven counter-propagating OMEGA platform was designed to be

flexible enough to allow the investigation of different flow conditions and physics package geometries, without reconfiguring the drive lasers or diagnostics.²⁸ Indeed, the reshock and shear experiments have been carried out using the same basic shock tube setup.²⁸ The resulting datasets have been used to verify²⁸⁻²⁹ the parameters of the BHR turbulence model³⁷ in an HED environment as implemented in the Los Alamos National Laboratory (LANL) Eulerian code, RAGE,³⁸ to provide the validation data for development of new techniques in large-eddy-simulations,³⁹ and to study the physics of thermal-turbulence coupling.³⁰

Recently, this LANL experimental testbed at OMEGA has been scaled up to the National Ignition Facility (NIF) with an indirectly-driven shock tube.⁴⁰⁻⁴¹ The extended shock tube length, coupled with the available stronger drive and advanced diagnostic capabilities, created a high-energy-density hydrodynamics platform of unprecedented scale. The counterpropagating shear experiment was again fielded to maximize the driving time of the hydrodynamic system. Two-dimensional (2D) postshot and design radiation hydrodynamics simulations were performed with the RAGE code.

In this paper, we perform both 2D and 3D simulations of the NIF counterpropagating shear experiments. In section 2, we review the experiments, and discuss the models and simulations. In section 3, we show that with an appropriate initial condition, the results from 2D and 3D mix calculations using a three-equations turbulence model agree well with the experimental measurements. In section 4, we use the simulated 3D dataset to illustrate a late-time three-dimensional edge-effect that can not be studied in a 2D only setting. We conclude with a summary. Details of our analysis are provided in two appendices.

2. Formulation of the physical problem

The experimental counterpropagating shear data have been collected from the new NIF platform pictured in Figure 1. Doss et al.⁴⁰ and Flippo et al.⁴¹ discussed the superior drive capabilities of the NIF and the reader is referred to those papers for a detailed account.

Briefly, the x-ray drive from the laser cavities produce shocks with 130 $\mu\text{m}/\text{ns}$ velocities, 10 Mbar post-shock pressures, and 110 $\mu\text{m}/\text{ns}$ post-shock flow speeds. The shock tubes, now 5.2 mm long and 1.5 mm ID, are filled with the same 60 mg/cc foam. After the lasers are applied to the both ends, shock waves are launched into the system. The ablator material is prevented from propagating down half of the tube by a hemicylindrical Au block, which allows the shock to enter the foam in only half of the tube. After the Au blocks on each end, the shocks are separated by an aluminum plate, and later the shocks cross in the center of the tube creating a pressure-balanced shear-induced mix region in the center area. In a modification from the OMEGA experiments, the tube is fitted with gold halfraums on either end, which use the cylindrically symmetric beam arrangement at the NIF in a natural manner – the target is aligned vertically in the chamber. As discussed in Refs. 40-41, this indirect-drive arrangement allows for longer lived hydrodynamics and a cleaner implementation of the desired physics by delaying rarefactions and pressure drops. The longer run times also allow for possible access to the turbulent regime.²⁰⁻²²

The 2D and 3D simulations reported in this paper were carried out by a Lawrence Livermore National Laboratory (LLNL) three-dimensional, time dependent radiation hydrodynamics simulation code KULL.⁴² Most importantly, KULL is particularly appropriate for our efforts, as this code models an experiment in full three dimensions with a capability to handle multi-materials and moving boundaries through an arbitrary Lagrangian Eulerian (ALE) formulation. By using both Lagrangian and Eulerian formulations, material interfaces can be tracked accurately with nodes placed on material boundaries, and strong shearing and vortical motions can be modeled as well. The radiation flow is accurately modeled by S_N radiation transport method with multiple energy groups⁴³. Another interesting feature is that KULL's mesh or zoning scheme also differs from most other codes of this type, as it supports an unstructured mesh of arbitrary polyhedra.^{42,44}

In our simulations, five materials are used to represent the polystyrene ablator with 2% silicon, the plastic shock tube, the gold block, the foam, and the aluminum (Al) tracer layer (Fig. 2a). An air wrap around the shock tube is added to the computational domain to make the numerical modeling easier since the boundary condition for air can be easily

set up and all other internal material interfaces will be handled by the code due to its ability to track the material interfaces using the ALE method. The total numbers of the zones used are 2.8 million for 3D and 66,000 for 2D, respectively. The minimum zone size is $2.5\text{ }\mu\text{m}$. Because of the code flexibility and capability, we were able to model our experiments in a full 3D geometry with all physics included by an optimal 3D mesh, which has high resolutions in the regions of interest (Fig. 2b).

The turbulence model implemented in KULL and utilized in this study is a standard Reynolds Averaging Navier-Stokes (RANS) model. This most updated model combines the traditional K - L model⁴⁵⁻⁴⁶ with a transport equation for the mass flux.³⁷ This K - L - a three-equation turbulence model consists of the evolutionary equations for the turbulent kinetic energy per unit mass, K , the equivalent turbulent length scale L , and the mass flux, a . The performance of this turbulence model has been tested extensively and the model equations are in fact quite similar to those of the BHR model.³⁷ Using several benchmark laboratory experiments, the coefficients of this RANS model have been determined. The only adjustable parameter is the initial length scale, L_0 .

3. Layer width computations

The high-energy x-ray emissions from the hohlraum upstream in the experiment, which determines the effective preheat, was estimated around 0.5 eV at the tube center.⁴⁰⁻⁴¹ The simulation is driven by a radiation temperature source based a post-shot halfraum simulation of NIF shot *NI40117*. In this simulation, the energy delivered to the two halfraums differed by $\sim 10\%$, resulting in a difference in peak radiation temperature of about 3%. (Fig. 3). Launching shocks of equal strength from both ends of the shock tube has at least two important benefits. First, a useful simplification can be achieved by the symmetry of the experiment to use the data for testing the RANS model, since the pressure gradient across the mixing layer can be eliminated.³⁰ Second, it is shown in the next section that the edge effects from the 3D geometry, which can confuse the measurement at late times, can be reduced or even eliminated. In Appendix A, we illustrate this undesirable feature with a sensitivity study using two alternative

asymmetric drives. It was found that there is a strong edge effect when the radiation temperature difference between the drives is increased to 10%.

To justify the use of a radiation temperature source in the simulations, a shock timing check was conducted. The experimental data indicated that at 17.6 ns, the shocks launched from opposite ends of the shock tube are directly opposite each other. Fig. 4 shows that the 2D and 3D simulations at $T = 17.6$ ns can accurately reproduce this shock-timing. Furthermore, turning on the turbulence mix model essentially does not have any impact on this case: the difference between the shock-timing is a mere 0.1 ns.

The “clean” layer widths are first given for both the 2D and 3D simulations in Fig. 5. These curves are obtained from the KULL simulations with the $K-L-a$ model turned off. The shocks cross the central region around 17 ns. In those simulations, three phases for the Al tracer are noticeable: the preheat phase, the compression phase, and the layer expansion phase. In the clean simulations, as well as in the 2D mix simulations, we also observe recompression of the expanded layer after the compression phase as a result of reflected waves in the system, and as reported in an early counterflowing shear study.³⁰

In Fig. 5, the NIF experimental mixing layer widths, which are defined by looking for x-ray {or radiographic} absorption over a pre-defined threshold, are shown for comparison with the numerical model. The detailed experimental data analysis is given in Appendix B, but for a given image, the definition of the mixing layer width depends on the contrast that results from backlighter brightness and tube attenuation which may vary from shot-to-shot. This approach is appropriate for the NIF measurements as the noise of the radiograph is low. Using VisIt, an open source application for data analysis and visualization, the simulated mix widths are obtained by measuring the distance at the middle of the tracer strip.

As mentioned already, the turbulence model has a single adjustable parameter. Here, in terms of the $K-L-a$ model, this parameter, L_0 , is the length scale at the starting time of the simulations. Conceptually, L_0 can be viewed as a parameter that is related to the initial roughness of the interfaces. A goal of these high-energy-density physics experiments is to provide the data needed for turbulence model development. As demonstrated in Fig. 5,

the results of the 2D and 3D mix width agree reasonable well with the experimental data when $L_0 = 0.5 \times 10^{-4}$ (cm) and 10^{-5} (cm), respectively.

In Fig. 6, we show the sensitivity of the mix width development on the input parameter L_0 . It is interesting that the mixing layer width is observed to briefly spike due to a “dust-up” effect behind the shock for several values of the initial parameter, L_0 , in both 2D and 3D. Based on those data, the transition value of L_0 from a compression phase to a “dust-up” phase is around 10^{-5} for the 3D model, and the 2D model requires a larger L_0 to reach this transition. This “dust-up” behavior was previously observed in the LANL OMEGA experiments (Fig. 4 and 6 of Ref. 29) and it was apparently due to sudden deposition of vorticity on the layer surface as the shock passes, triggering mixing of aluminum into foam. After this brief dust-up, in the turbulent simulation, the shear instability leads to uniform growth of the layer mix width. Plotting the Al tracer layer material and the plastic tube explicitly, Fig. 7 shows that the dust-up behavior is found in both 2D and 3D with $L_0=10^{-3}$. In order to match the observed dust-up feature, Doss et. al. required, in addition to a high L_0 , that the species transport equation in RAGE be active.³⁰ However, as neither subsequent Omega experiments³⁰ nor the NIF experiments⁴⁰⁻⁴¹ produced a dust-up feature as prominent as in Ref. 29, it is possible the feature is related to the specific initial condition of the targets used in that series, a more bumpy Al tracer layer that was vapor deposited directly on the foam, which a RANS model would not capture accurately. Additional counterpropagating shear experiments on NIF are being considered with different tracer materials, thicknesses and surface roughnesses, to study the effect of the surface initial condition, and also the density of the tracer material, on the turbulent mixing.⁴⁷

To provide an instantaneous snapshot to be directly compared with experimental data, simulated radiographs have been produced from the KULL datasets. The simulated images depend on the backlighter energy as well as the user-input x-ray opacities. In Fig. 8, we compare our 2D and 3D simulated radiographs, using KULL data from the turbulence model (with $L_0=0.5 \times 10^{-4}$), with the experimental data at 17.6 ns, 21.8 ns, and

28.4 ns. They agree satisfactorily.

4. Edge and late-time end-effects

In Fig. 9, we examine the issue of the edge effect with our 3D simulation data at two different times, 22 ns and 28 ns. Recall that the drive used here is derived from the experimental data *N140117*, for which the peak radiation drive temperatures at the ends of the tube differ by $\sim 3\%$. At this level of asymmetry, the shocks are still essentially of equal strength. It is evident that edge effects are not important for the system with a nearly symmetric energy drive. In Appendix A, we illustrate how edge effects become pronounced as the temperature asymmetry is increased to 10%.

The late time end-effect from materials moving toward the shock tube center can be examined from the 2D and 3D material plots at 28.4 ns (Fig. 10). In order to isolate the physics, these plots are produced from the "clean" calculations so that the turbulence model influences are sidestepped. The end-effect can be easily identified from the tube and Al tracer material, and some of the tube material is forced to move to the shock tube center by the flow. 3D data show the end-effect clearly, but 2D data show less influence of the tube material in the center due to the 2D numerical assumption. The aluminum tracer layer material is shown at late time (28.4 ns) in Fig. 11 for both the clean and turbulent (with $L_0=10^{-3}$) calculations at 2D and 3D. As shown in Fig. 11 (as well as the rightmost, bottom picture of Fig. 7), the 3D mix width is decreased with the end-effect (tube) material pushed in from both sides of the tracer layer.

Furthermore, it should be noted that the experimental radiography would not be able to properly distinguish the shadowy areas identified from the simulated 3D Al tracer layers (as illustrated in Fig. 11). Fortunately, this artifact still does not have significant impact at 28.4 ns on the mix width measurement, which is taken at the middle of the tracer layer. To show the end-effect from the tube material, as well as that from a mix model, the 2D and 3D simulated radiographs are presented in Fig. 12 from the clean and turbulent calculations (with $L_0 = 0.5 \times 10^{-4}$).

5. Summary

In this paper, a time-dependent radiation hydrodynamics simulation code is used to perform two- and three- dimensional numerical simulations of the recent National Ignition Facility (NIF) counterpropagating shear flow experiments. The experiments provided the data to calibrate the initial condition of a Reynolds Averaging Navier-Stokes (RANS) model, and our numerical model was used to investigate the geometry effects at late times. The L_0 parameter of the RANS model was determined so that the evolution of the mixing layer width obtained from the simulations would agree with that measured from the experiments. No late-time edge-effect is found when the drives from the two ends of the shock tube are symmetric to within 3% in peak radiation temperature. When the drive asymmetry is increased to 10% in peak radiation temperature, however, the edge-effect is pronounced. These numerical results provided useful information for future experimental designs.

Acknowledgments

The authors are indebted to John L. Kline and Barbara DeVolder for their contributions, as well as the LLNL colliding shock experiment group and LLNL ASC code group for their assistance. We would like to thank Mark S. Ulitsky for his suggestion on the parameter setting of the K-L-a mix model. We thank Brett Friedman, Tanim S. Islam and Oleg Schilling for stimulating discussions. This work was performed under the auspices of the U.S. Department of Energy by Lawrence Livermore National Laboratory under Contract No. DE-AC52-07NA27344. This work was also supported by the U.S. Department of Energy and performed by Los Alamos National Laboratory, operated by Los Alamos National Security under Contract No. DE- AC52-06NA25396.

Appendix A: Sensitivity to the drive asymmetry

In this appendix, we investigate the sensitivity of the edge-effect to the drive asymmetry between the shocks from two ends of the shock tube. Another temperature source, which was obtained by scaling an experiment's DANTE^{49,50} data, will be used for this investigation (Fig. A1). The temperature asymmetry for this synthetic shot is set to be 10%. Fig. A2 provides an illustration on how the different shock strengths have resulted in the edge-effect for the Al tracer layer at 22 ns (from a clean calculation with $L_0 = 10^{-3}$).

To demonstrate the 3D edge-effect on Al tracer layer more clearly, the material plots of the layer were given at both 22 ns and 28 ns in Fig. A3 from the clean (left) and mix (right) calculations. The edge-effect in this case is very clear and this case should be compared and contrasted to that of Fig. 9, where the temperature drive asymmetry was at a mere 3%. In fact, the contribution to the mix widths from the edge-effect is comparable with that from the mix model with $L_0 = 10^{-3}$. For a smaller L_0 setting, the edge-effect would have relatively stronger impact on the width measurement. The significant edge effect can also be viewed using the simulated radiograph (Fig. A4), where the tracer layer in 3D clean calculation is significantly thicker than that of 2D clean one. Under these conditions of temperature drive asymmetry, the Al tracer width measurements from the radiographs of the experiments will be affected by those edge-effects. The reason is that even this small path length of aluminum, circled in Fig. A2, has significant optical depth to the ~ 6.2 keV x-rays used to image the target. It is possible that using harder x-rays or a tracer layer approach, as in Refs. [23-27] (and many other HED instability experiments), could mitigate this effect. We point out that 3D edge effects of this type, related to the integrating nature of radiography methods, have also been noted (Ref. 48) in the shear platform used in Refs. [23-27]. Notches of approximately 50 microns depth have been added inside the target walls into which the foil fits to further mitigate any edge effects in the experiments.

Appendix B. Detailed data analysis from the experiments

The temporal evolution of the tracer width used for comparison to the RANS model was measured from a series of experiments, each capturing an x-ray image of the system at two times. An example x-ray radiograph is shown in Fig. B1.a. The ~ 6.2 keV x-rays from an iron He- α source are attenuated by the unshocked tube walls (indicated by item (1) in B1.a), and more strongly where the shock has compressed the plastic wall (item (2)). The tracer layer (item 3), initially centered in the tube, is distorted by the opposing shocks, which are traveling up on the left side of the tracer strip and down on the right side. The middle of the tracer strip remains nearly vertical because the pressure from each of the shocks is opposed by the other, and it is this region that we used for the width analysis.

A unique region of interest (ROI) was selected for each frame, given by the blue box in Fig B1.a for this frame. An edge-detection calculation was performed, using the same threshold value for each image. In this way the edges of the tracer strip were identified within the ROI, as shown in Fig. B1.b. The tracer strip width was calculated by measuring the shortest distance between edges *perpendicular to the tube axis* for each pixel in the vertical direction. These measurements are shown as horizontal gray bars between the identified edges in Fig. B1.c, and the values presented in Figs. 5 and 6 are the average of all of the measurements at a single time.

References:

1. O.M. Phillips, *Annu. Rev. Fluid Mech*, (1969) 245
2. A.A.R. Townsend, *The Structure of Turbulent shear flow* (Cambridge Univ Press, 1980)
3. Lord Kelvin, *Philosophical Magazine*, 42 (1871) 362
4. H. von Helmholtz, *Philosophical Magazine Series 4*, 36 (244), 1868
5. P.G. Drazin and W.H. Reid. *Hydrodynamic Stability*. (Cambridge, MA: Cambridge Univ. Press, 1981).
6. W. R. Peltier and C. R. Caulfield, *Annu. Rev. Fluid Mech.* **35** (2003) 135
7. J.D. Woods, *J. Fluid Mech.* **32** (1968) 791
8. J. D. Lindl, *Phys. Plasmas*, 2, (1995) 3933
9. Lord Rayleigh, *Proc. London Math. Soc.* **14**, (1883) 170
10. G. I. Taylor, *Proc. R. Soc. London, Ser. A* 201, (1950) 192
11. R. D. Richtmyer, *Commun. Pure Appl. Math.* **13**, (1960) 297
12. E. E. Meshkov, *Sov. Fluid Dyn.* **4**, (1969) 101
13. S. W. Haan, J. D. Lindl, D. A. Callahan, D. S. Clark, J. D. Salmonson, B. A. Hammel, L. J. Atherton, R. C. Cook, M. J. Edwards, S. Glenzer, A. V. Hamza, S. P. Hatchett, M. C. Herrmann, D. E. Hinkel, D. D. Ho, H. Huang, O. S. Jones, J. Kline, G. Kyrala, O. L. Landen, B. J. MacGowan, M. M. Marinak, D. D. Meyerhofer, J. L. Milovich, K. A. Moreno, E. I. Moses, D. H. Munro, A. Nikroo, R. E. Olson, K. Peterson, S. M. Pollaine, J. E. Ralph, H. F. Robey, B. K. Spears, P. T. Springer, L. J. Suter, C. A. Thomas, R. P. Town, R. Vesey, S. V. Weber, H. L. Wilkens, and D. C Wilson, *Phys. Plasmas.* **18**, (2011) 051001
14. V.A. Thomas and R.J. Kares, *Phys. Rev. Lett.*, 109 (2012) 075004
15. V. A. Smalyuk, D.T. Casey, D. S. Clark, M. J. Edwards, S. W. Haan, A. Hamza, D. E. Hoover, W. W. Hsing, O. Hurricane, J. D. Kilkenny, J. Kroll, O. Landen, A. Moore, A. Nikroo, L. Peterson, K. Raman, B. A. Remington, H. F. Robey, S. V. Weber, and K. Widmann, *Phys. Rev. Lett.* **112**, 185003 (2014).
16. K. S. Raman, V. A. Smalyuk, D. T. Casey, S. W. Haan, D. E. Hoover, O. A.

- Hurricane, J. J. Kroll, A. Nikroo, J. L. Peterson, B. A. Remington, H. F. Robey, D. S. Clark, B. A. Hammel, O. L. Landen, M. M. Marinak, D. H. Munro, K. J. Peterson, and J. Salmonson. *Phys. Plasmas* 21, 072710 (2014).
17. V. A. Smalyuk, R. E. Tipton, J. E. Pino, D. T. Casey, G. P. Grim, B. A. Remington, D. P. Rowley, S. V. Weber, M. Barrios, L. R. Benedetti, D. L. Bleuel, D. K. Bradley, J. A. Caggiano, D. A. Callahan, C. J. Cerjan, D. S. Clark, D. H. Edgell, M. J. Edwards, J. A. Frenje, M. Gatu-Johnson, V. Y. Glebov, S. Glenn, S. W. Haan, A. Hamza, R. Hatarik, W. W. Hsing, N. Izumi, S. Khan, J. D. Kilkenny, J. Kline, J. Knauer, O. L. Landen, T. Ma, J. M. McNaney, M. Mintz, A. Moore, A. Nikroo, A. Pak, T. Parham, R. Petrasso, D. B. Sayre, M. B. Schneider, R. Tommasini, R. P. Town, K. Widmann, D. C. Wilson, and C. B. Yeamans, *Phys. Rev. Lett.*, 112 (2014) 025002
 18. T. Yabe, H. Hoshino, and T. Tsuchiya, Two- and three-dimensional behavior of Rayleigh–Taylor and Kelvin-Helmholtz instabilities, *Phys. Rev. A*, 44, (1991) 2756
 19. N. J. Zabusky, *Annu. Rev. Fluid Mech.* 31, (1999) 495
 20. Y. Zhou, B. A. Remington, H. F. Robey, A. W. Cook, S. G. Glendinning, A. Dimits, A. C. Buckingham, G. B. Zimmerman, E. W. Burke, T. A. Peyser, W. Cabot, and D. Eliason, *Phys. Plasmas*, 10, (2003) 1883
 21. Y. Zhou, H. F. Robey, and A. C. Buckingham, *Phys. Rev. E*, 67 (2003) 056305.
 22. Y. Zhou, *Phys. Plasmas*, 14 (2007) 082701.
 23. E. C. Harding, J. F. Hansen, O. A. Hurricane, R. P. Drake, H. F. Robey, C. C. Kuranz, B. A. Remington, M. J. Bono, M. J. Grosskopf, and R. S. Gillespie, *Phys. Rev. Lett.* 103, 045005 (2009).
 24. O. A. Hurricane, J. F. Hansen, H. F. Robey, B. A. Remington, M. J. Bono, E. C. Harding, R. P. Drake, and C. C. Kuranz. *Phys. Plasmas*, 16 (2009) 056305
 25. O. A. Hurricane, J. F. Hansen, E. C. Harding, V. A. Smalyuk, B. A. Remington, G. Langstaff, H.-S. Park, H. F. Robey, C. C. Kuranz, M. J. Grosskopf, R. S. Gillespie, Blast-wave driven Kelvin-Helmholtz shear layers in a laser driven high-energy-density plasma, *Astrophys. Space Sci.*, 336 (2011) 139
 26. O. A. Hurricane, V. A. Smalyk, K. Raman, O. Schilling, J. F. Hansen, G.

- Langstaff, D. Martinez, H.-S. Park, B. A. Remington, H. F. Robey, J. A. Greenough, and R. Wallace, C. A. Di Stefano, R. P. Drake, D. Marion, C. M. Krauland, and C. C. Kuranz, *Phys. Rev. Lett.*, 109, (2012) 15
27. V.A. Smalyuk, O.A. Hurricane, J.F. Hansen, G. Langstaff, D. Martinez, H.-S. Park, K. Raman, B.A. Remington, H.F. Robey, O. Schilling, R. Wallace, Y. Elbaz, A. Shimony, D. Shvarts, C. Di Stefano, R.P. Drake, D. Marion, C.M. Krauland, C.C. Kuranz, *High Energy Density Phys.*, 9, (2013) 47
 28. L. Welser-Sherrill, J. Fincke, F. Doss, E. Loomis, K. Flippo, D. Offermann, P. Keiter, B. Haines, F. Grinstein, *High Energy Density Phys.*, 9 (2013) 496
 29. F W Doss, E N Loomis, L Welser-Sherrill, J R Fincke, K A Flippo, and P A Keiter. *Phys. Plasmas*, 20 (2013a) 012707
 30. F W Doss, J R Fincke, E N Loomis, L Welser-Sherrill, and K A Flippo. *Phys. Plasmas*, 20, (2013b) 122704
 31. E. Loomis, F. Doss, K. Flippo, and J. Fincke. *Phys. Plasmas*, 21:044508, 2014.
 32. G. L. Brown and A. Roshko, *J. Fluid Mech.* 64, (1974) 775
 33. C.-M. Ho and P. Huerre, *Annu. Rev. Fluid Mech.*, 16, (1984) 365
 34. D. Papamoshou, *Phys. Fluids* 7, 233 (1995).
 35. F. S. Alvi, A. Krothapalli, and D. Washington, *AIAA J.*, 34, (1996) 728
 36. P. J. Strykowski, A. Krothapalli, and S. Jendoubi, *J. Fluid Mech.*, 308, (1996) 63
 37. D. Besnard, F. Harlow, R. Rauenzahn, and C. Zemach, Technical Report LA-12303-MS, Los Alamos National Laboratory, (1992).
 38. M. Gittings, R. Weaver, M. Clover, T. Betlach, N. Byrne, R. Coker, E. Dendy, R. Hueckstaedt, K. New, W. R. Oakes, D. Ranta, and R. Stefan, *Comput. Sci. Discovery* 1, (2008) 015005
 39. Y. Zhou, Fernando F. Grinstein, Adam J. Wachtor, and Brian M. Haines. *Phys. Rev. E*, 89 (2014) 013303
 40. F. W. Doss, J. L. Kline, K. A. Flippo, T. S. Perry, B. G. DeVolder, I. Tregillis, E. N. Loomis, E. C. Merritt, T. J. Murphy, L. Welser-Sherrill, and J. R. Fincke, *Phys. Plasmas*, (2015) 22, 056303
 41. K. A. Flippo, F. W. Doss, B. DeVolder, J. R. Fincke, E. N. Loomis, J. L. Kline, L. Welser-Sherrill, *Journal of Physics: Conf. Series* (submitted)

42. J.A. Rathkopf, D.S. Miller, J.M. Owen, L.M. Stuart, M.R. Zika, P.G. Eltgroth, N.K. Madsen, K.P. McCandless, P.F. Nowak, M.K. Nemanic, N.A. Gentile, N.D. Keen, and T.S. Palmer, Technical Report UCRL-JC-137053, Lawrence Livermore National Laboratories, Livermore, CA, (2000).
43. P.F. Nowak and M.K. Nemanic, Technical Report UCRL-JC-133787, Lawrence Livermore National Laboratories, Livermore, CA, (1999).
44. J.M. Owen and M. Shashkov, J. Computational Phys. 273 (2014) 520
45. G.L. Mellor and H.J. Herring, AIAA J., 11 (1973) 590
46. D.C. Wilcox, Turbulence Modeling for CFD (DCW Industries, Inc, La Canada, CA, 1998).
47. E. C. Merritt, F. W. Doss, E. N. Loomis, K. A. Flippo, and J. L. Kline, Phys. Plasmas 22, 062306 (2015).
48. K. S. Raman, O. A. Hurricane, H.-S. Park, B. A. Remington, H. Robey, V. A. Smalyuk, R. P. Drake, C. M. Krauland, C. C. Kuranz, J. F. Hansen, and E. C. Harding, Phys. Plasmas 19, 092112 (2012).
49. J. L. Kline, K. Widmann, A. Warrick, R. E. Olson, C. A. Thomas, A. S. Moore, L. J. Suter, O. Landen, D. Callahan, S. Azevedo, J. Liebman, S. H. Glenzer, A. Conder, S. N. Dixit, P. Torres, V. Tran, E. L. Dewald, J. Kamperschroer, L. J. Atherton, R. Beeler, L. Berzins, J. Celeste, C. Haynam, W. Hsing, D. Larson, B. J. MacGowan, D. Hinkel, D. Kalantar, R. Kauffman, J. Kilkenny, N. Meezan, M. D. Rosen, M. Schneider, E. A. Williams, S. Vernon, R. J. Wallace, B. Van Wonterghem and B. K. Young, Rev. Sci. Inst. **81** (10) (2010).
50. E. L. Dewald, K. M. Campbell, R. E. Turner, J. P. Holder, O. L. Landen, S. H. Glenzer, R. L. Kauffman, L. J. Suter, M. Landon, M. Rhodes and D. Lee, Rev. Sci. Inst. **75** (10), 3759-3761 (2004).

Figure Captions:

Fig.1. The NIF target pictured, displaying (gray) the shock tube with enclosed metal plate with (yellow) gold plugs embedded on either end and a fiducial grid off at the bottom. The gold hohlraums on the left and the right launch indirect shock drive to the tube by driving the (brown) plastic ablator layer.

Fig. 2a. Sketch of the target geometry: a plastic tube containing foam with gold plugs is indirectly irradiated by two half-raums driven by lasers on both sides, launching shock waves into the system.

Fig. 2b. 2D and 3D meshes with five materials plus an air wrap.

Fig. 3. Temperature drives calculated from NIF shot N140117.

Fig. 4. Shock crossing times from both 2D and 3D calculations agree with the experimental time $t = 17.6$.

Fig. 5. Comparison of the simulation data in both 2D and 3D with the experimental data.

Fig. 6. The mix width measurements from the turbulence calculations depend on the initial condition, L_0 , the initial length scale. Various L_0 settings are used to study the sensitivity of this key parameter in the turbulence model.

Fig. 7. $K-L-\alpha$ model with a large $L_0 = 10^{-3}$ setting, and both 2D and 3D show the dust-up phase when the shocks cross.

Fig. 8. Simulated radiographs from 2D and 3D mix models are compared with the experimental films.

Fig. 9. The 3% difference from the temperature drives has no significant impact on the flow.

Fig. 10. The end-effect from the tube material is noticeable in the 3D (left) and 2D

(right) clean calculations, and the 3D simulation shows a stronger end-effect from the presence of the tube material in the middle of the shock tube.

Fig. 11. Al tracer layers are plotted from 2D and 3D simulations with both clean and mix ($L_0 = 10^{-3}$) models. The arrows indicate the shadowy areas of the simulated 3D Al tracer layers experimental radiography would not be able to properly distinguish.

Fig. 12. The radiographs of Al tracer with a time history from 2D and 3D simulations with both clean and mix models (with $L_0 = 0.5 \times 10^{-4}$).

Fig. A1. Dante drives from NIF shot N140117 with a 10% drive difference from both ends.

Fig. A2. An illustration of the edge-effects from the asymmetric drive.

Fig. A3. The 3D edge-effect on Al tracer are plotted on the left at $t = 22$ ns, 28 ns, and the Al growing widths from a mix model with $L_0 = 10^{-3}$ are plotted on the right.

Fig. A4. Simulated 2D and 3D radiographs show different tracer widths due to the edge-effect.

Fig. B1 (a): An x-ray image of the full tube width after shock crossing, approximately 23 ns. Labeled regions are (1) unshocked tube, (2) shocked tube wall, and (3) tracer layer. (b) Central tracer region of interest is shown, with identified edges. (c) The distance between edges is measured over the entire length of the ROI, given by the gray lines between the edges.

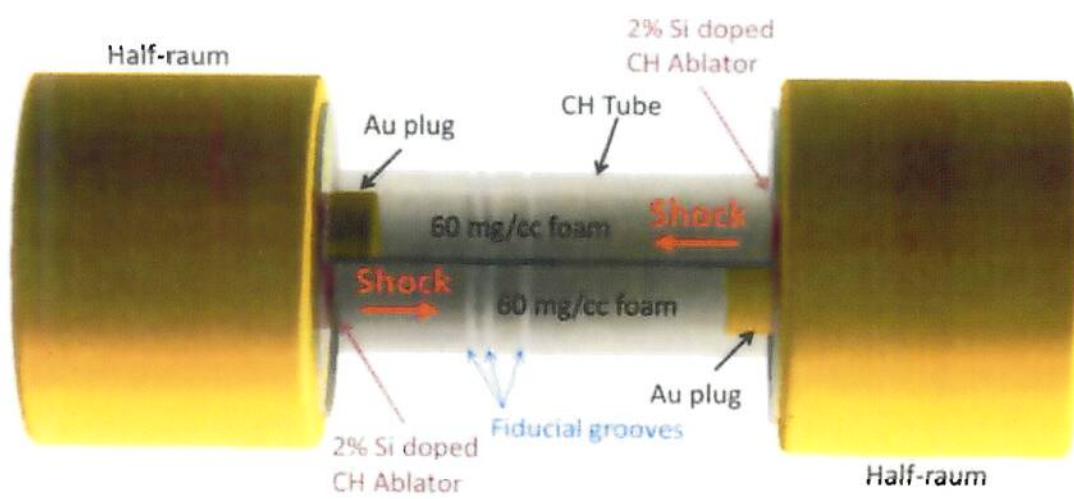


Fig. 1

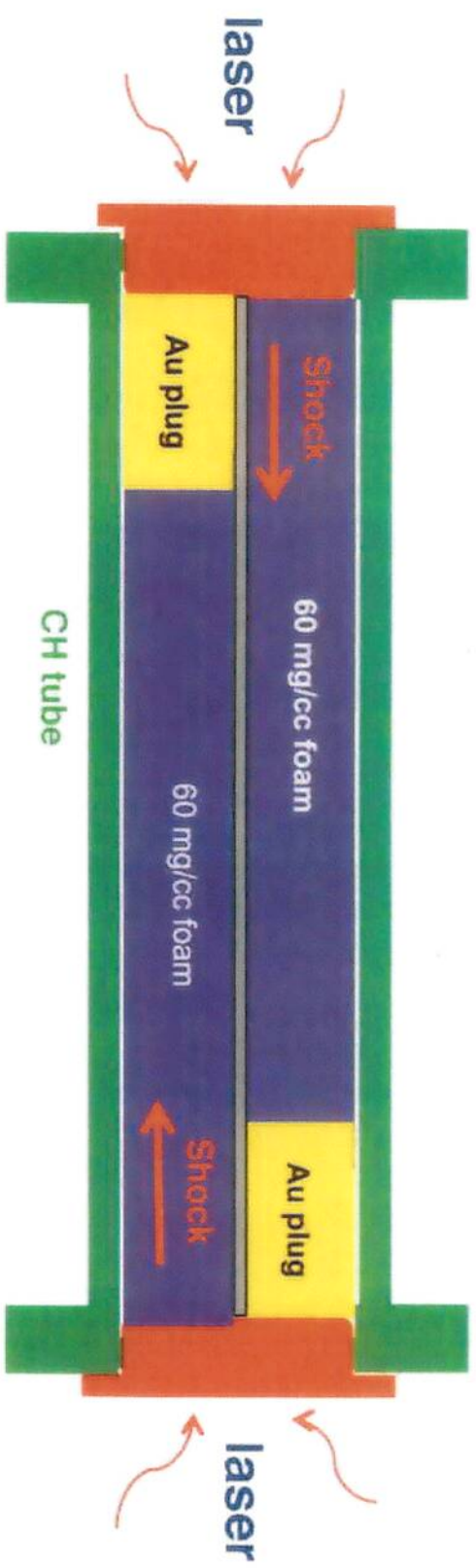


Fig. 2a

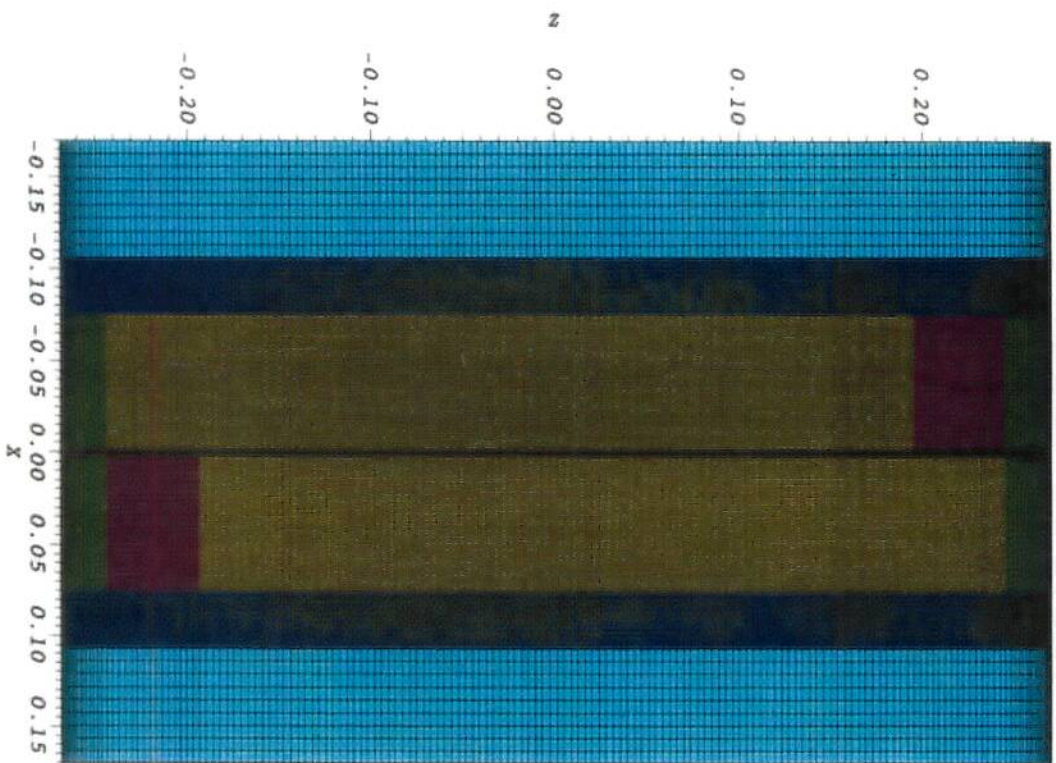


Fig. 2b

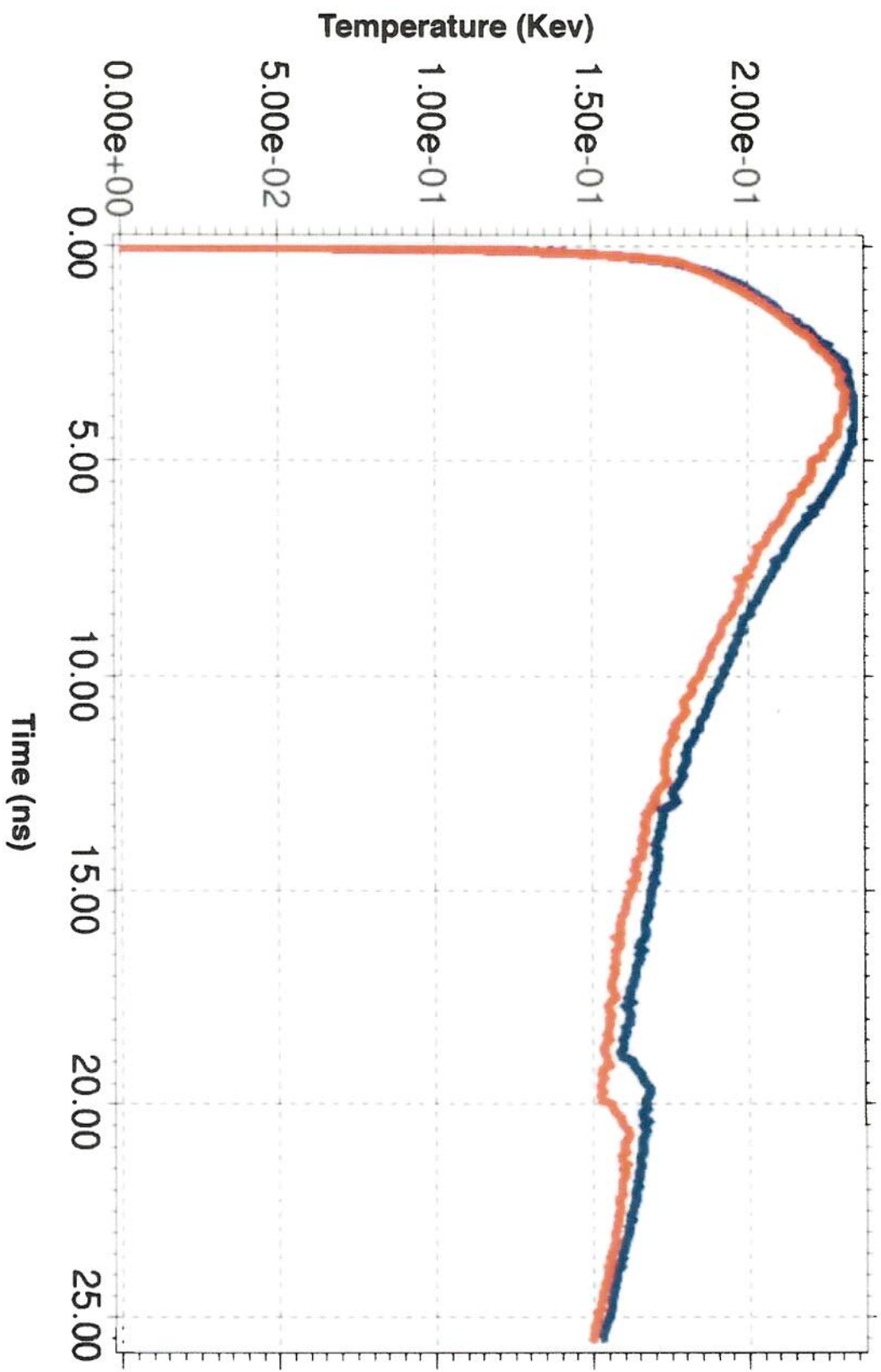
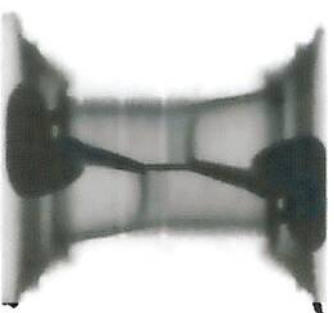
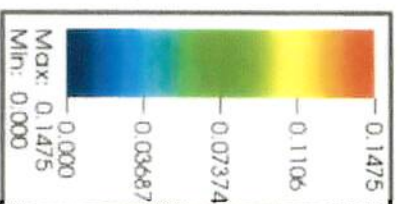
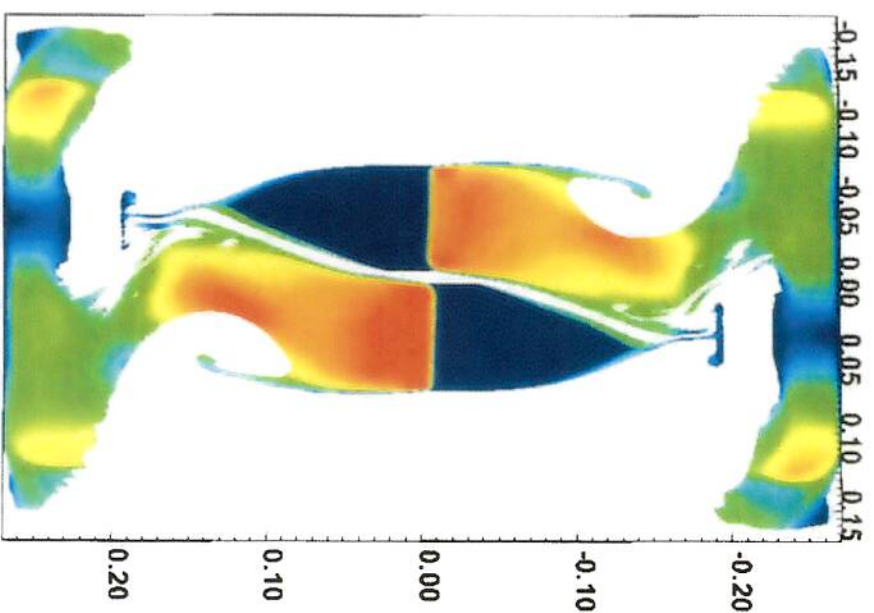


Fig. 3



LANL 2D data
at T = 17.6 ns

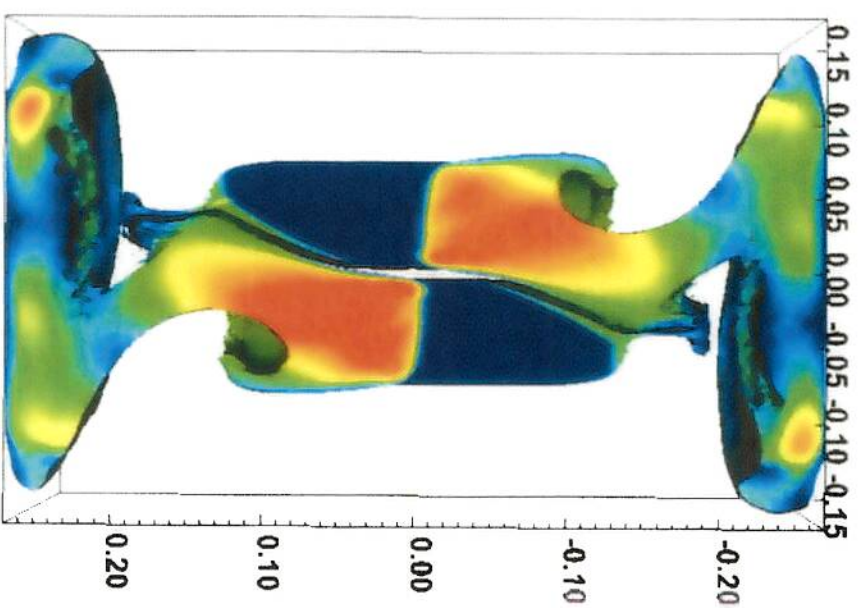


Fig. 4

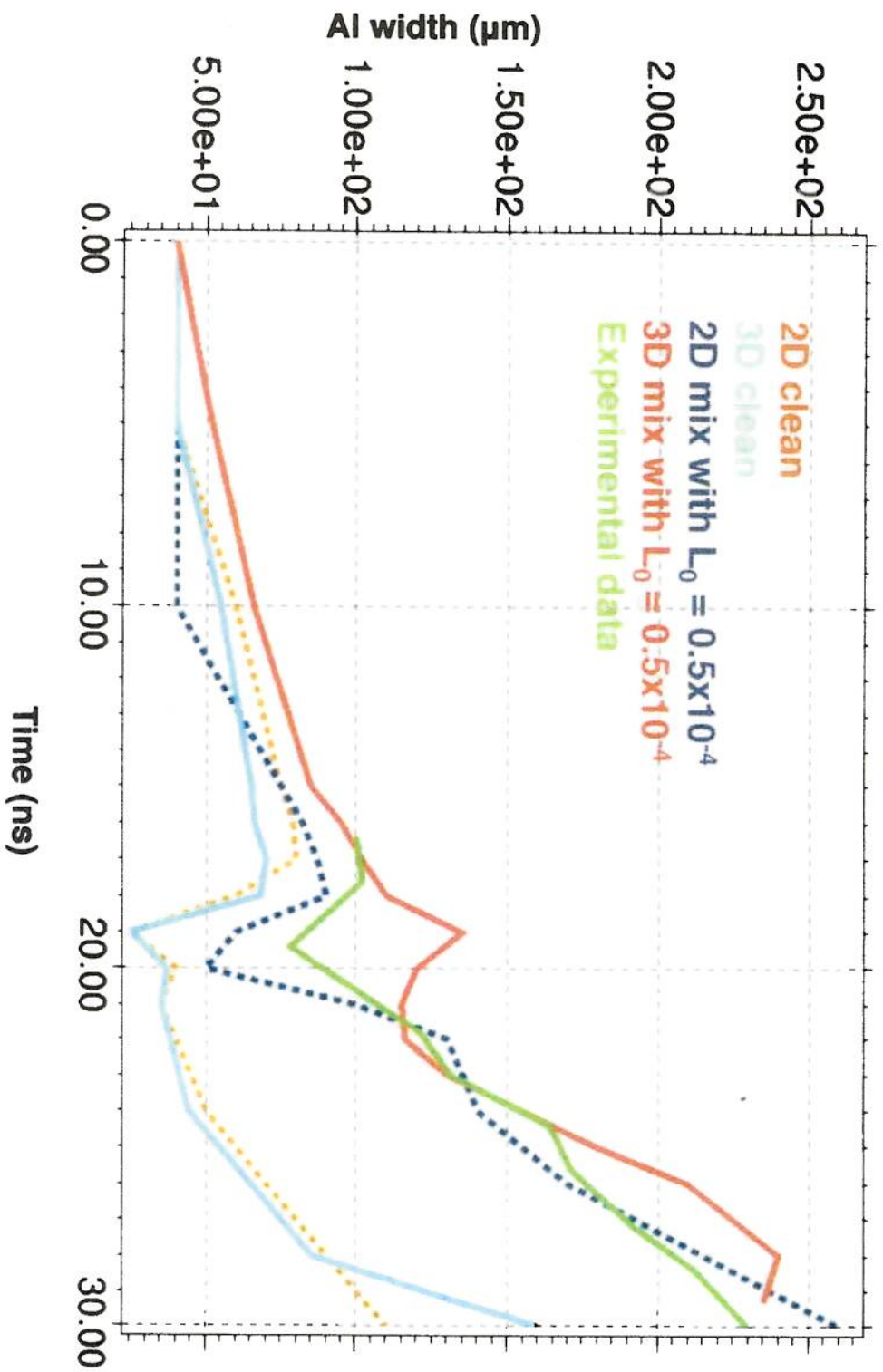


Fig. 5

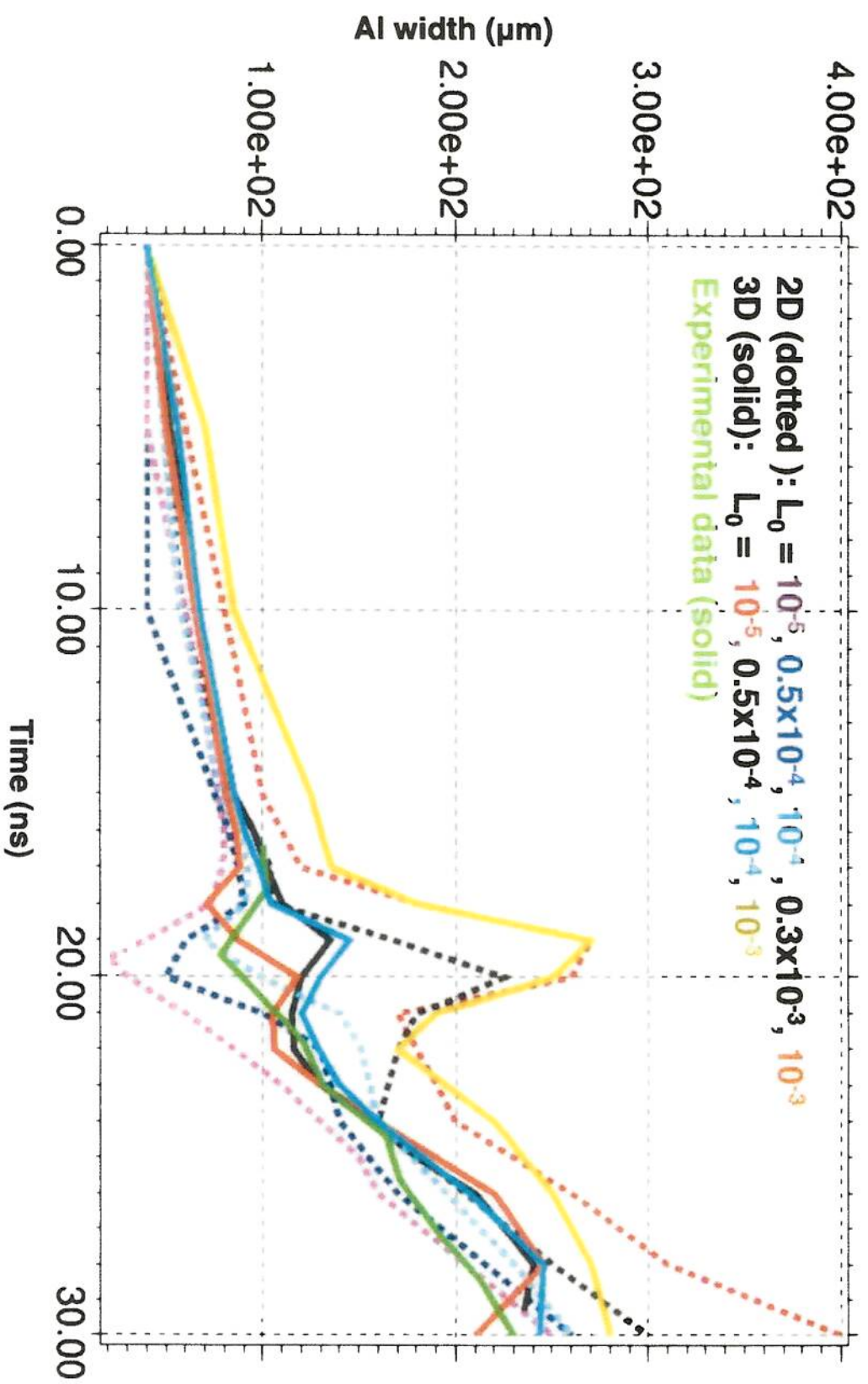
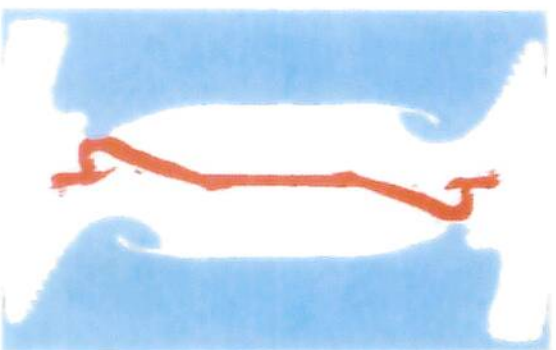
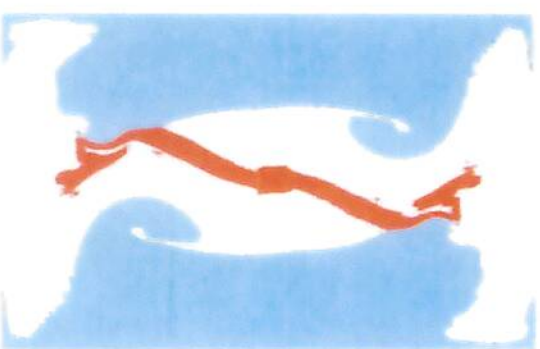


Fig. 6



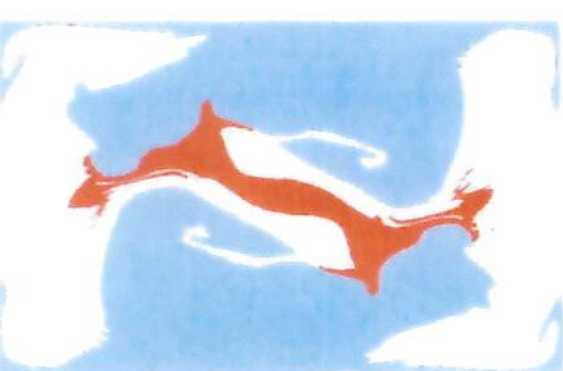
$T = 15 \text{ ns}$
Preheat



$T = 19 \text{ ns}$
Dust up



$T = 21 \text{ ns,}$
mix layer
growing



$T = 28.4 \text{ ns}$

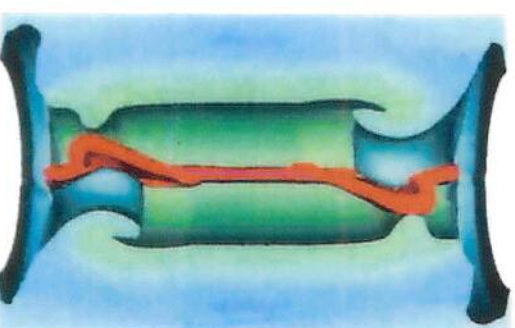


Fig. 7



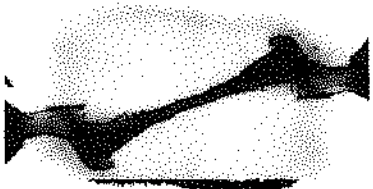
2D



3D



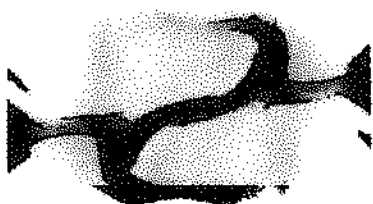
2D



3D



2D

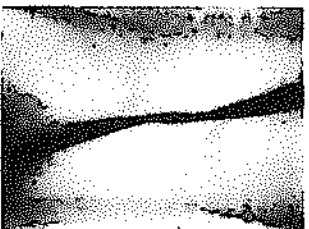


3D

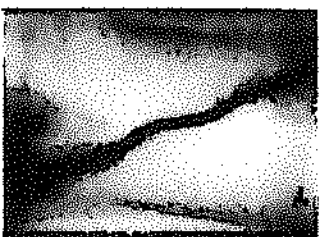
17.6 ns

21.8 ns

28.4 ns



HGXD Film



HGXD Film



HGXD Film

Fig. 8

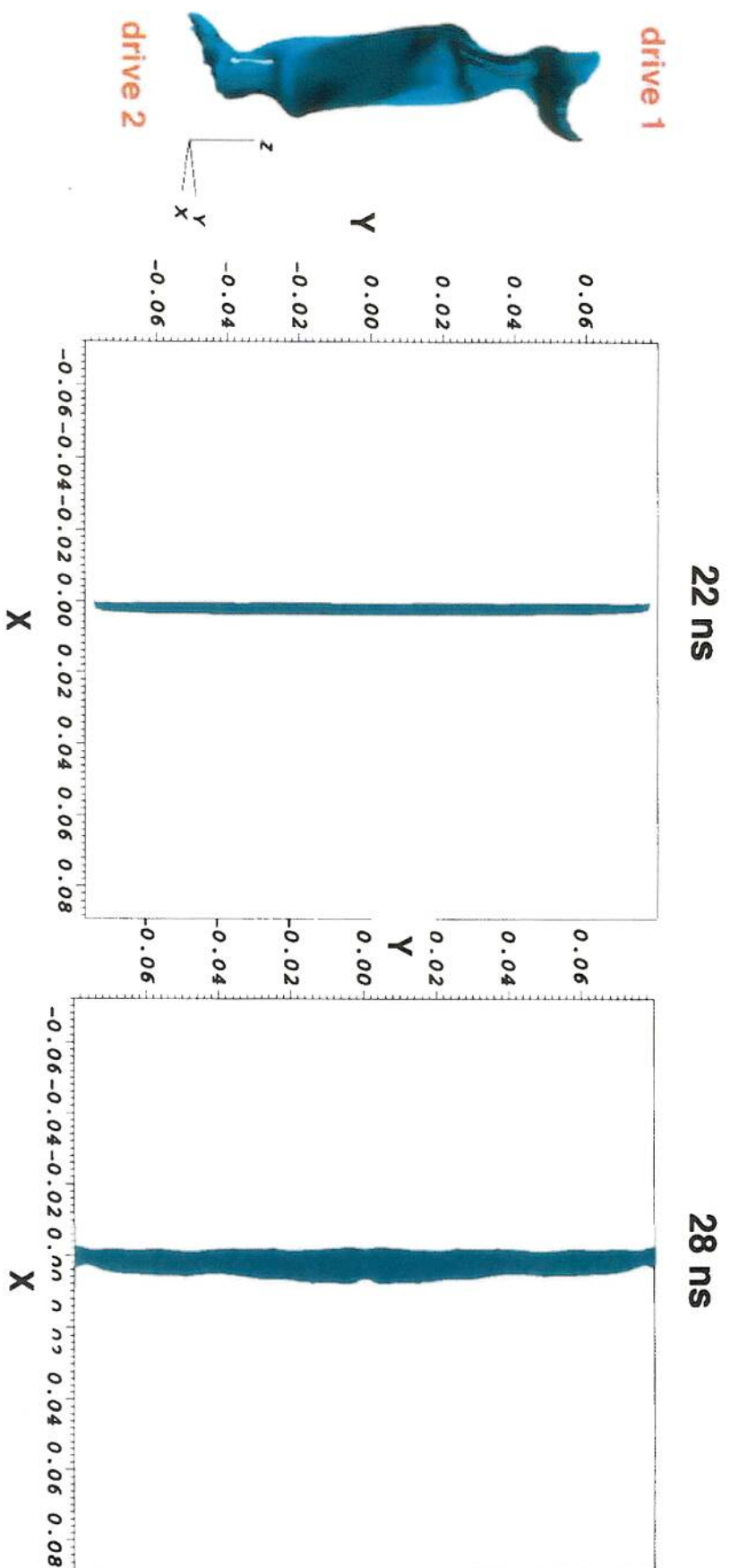


Fig. 9

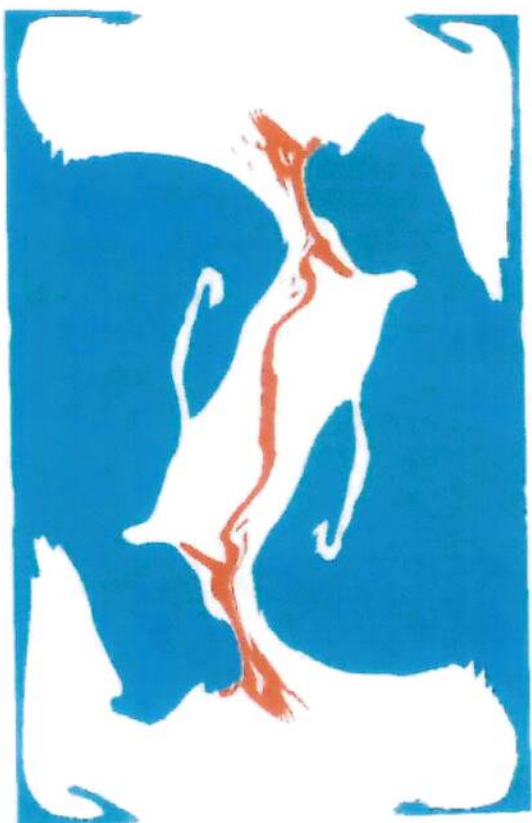


Fig. 10

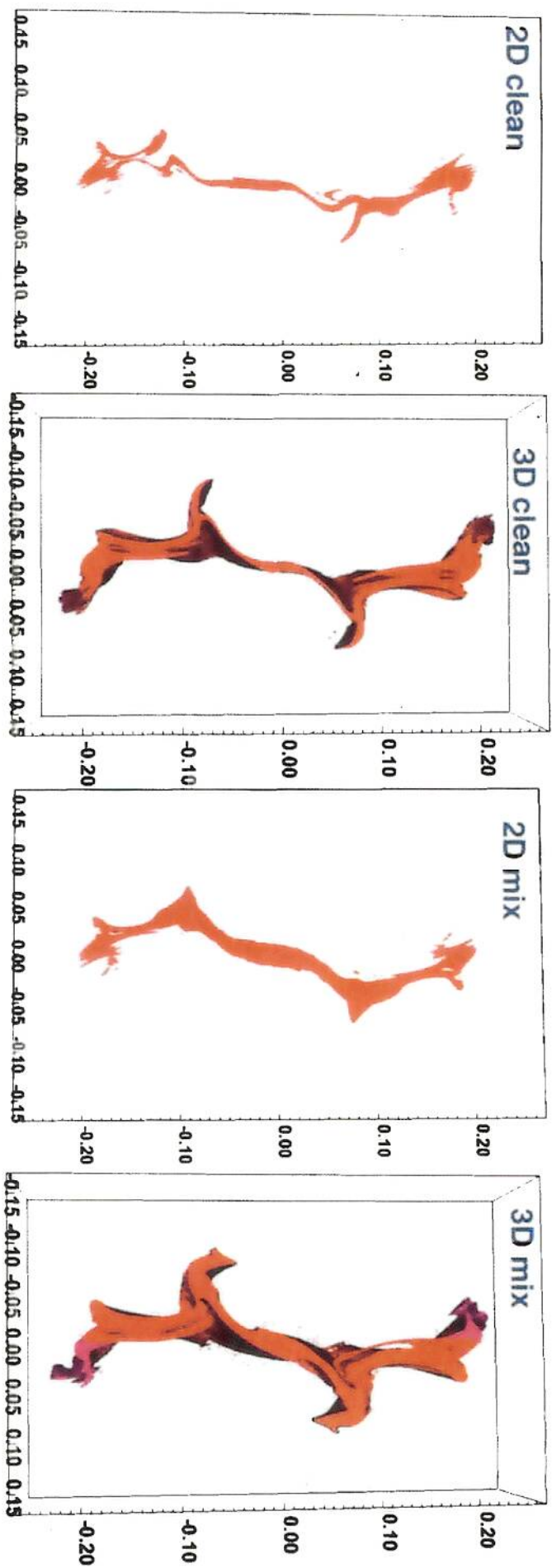


Fig. 11

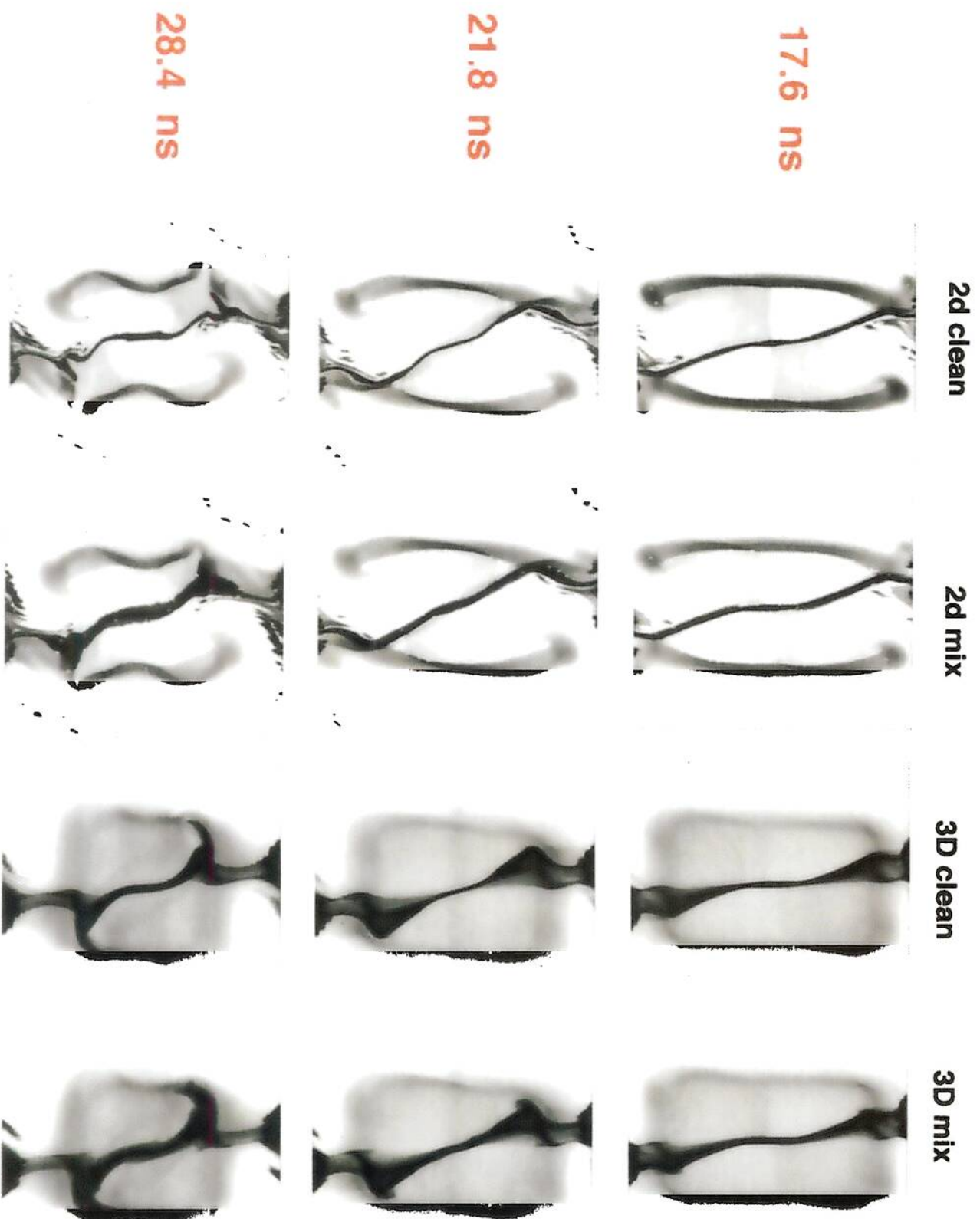


Fig. 12

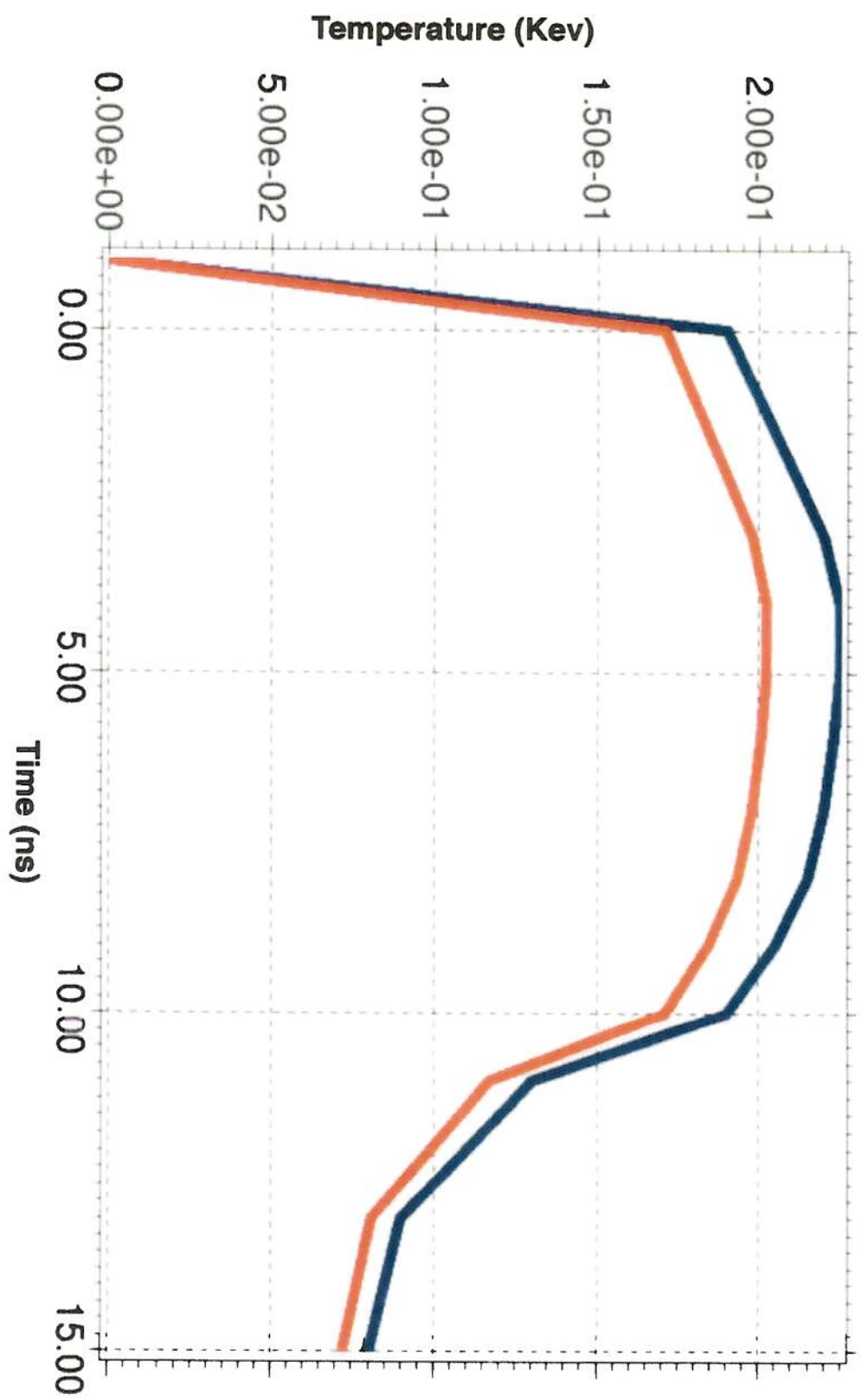


Fig. A1

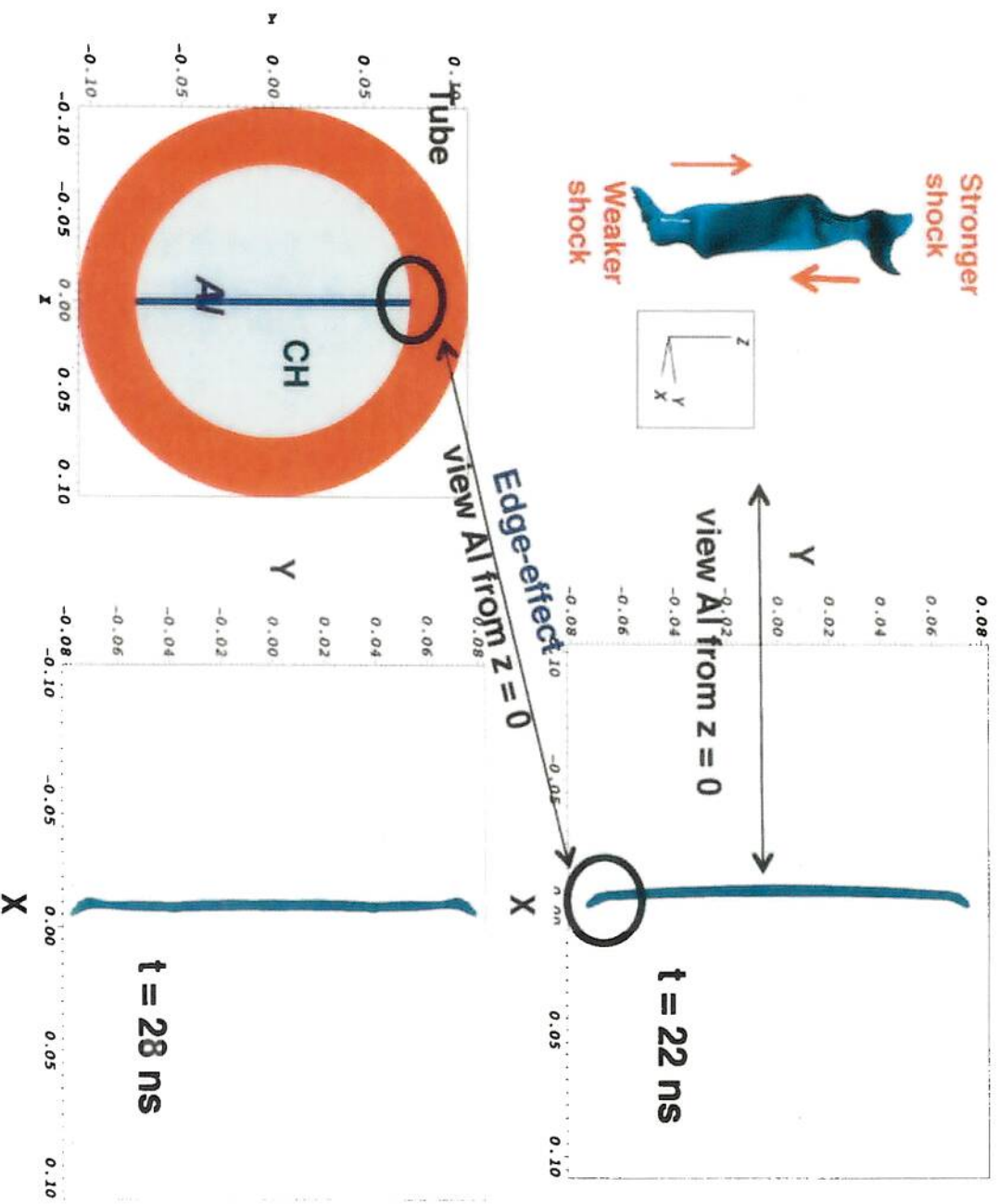


Fig. A2

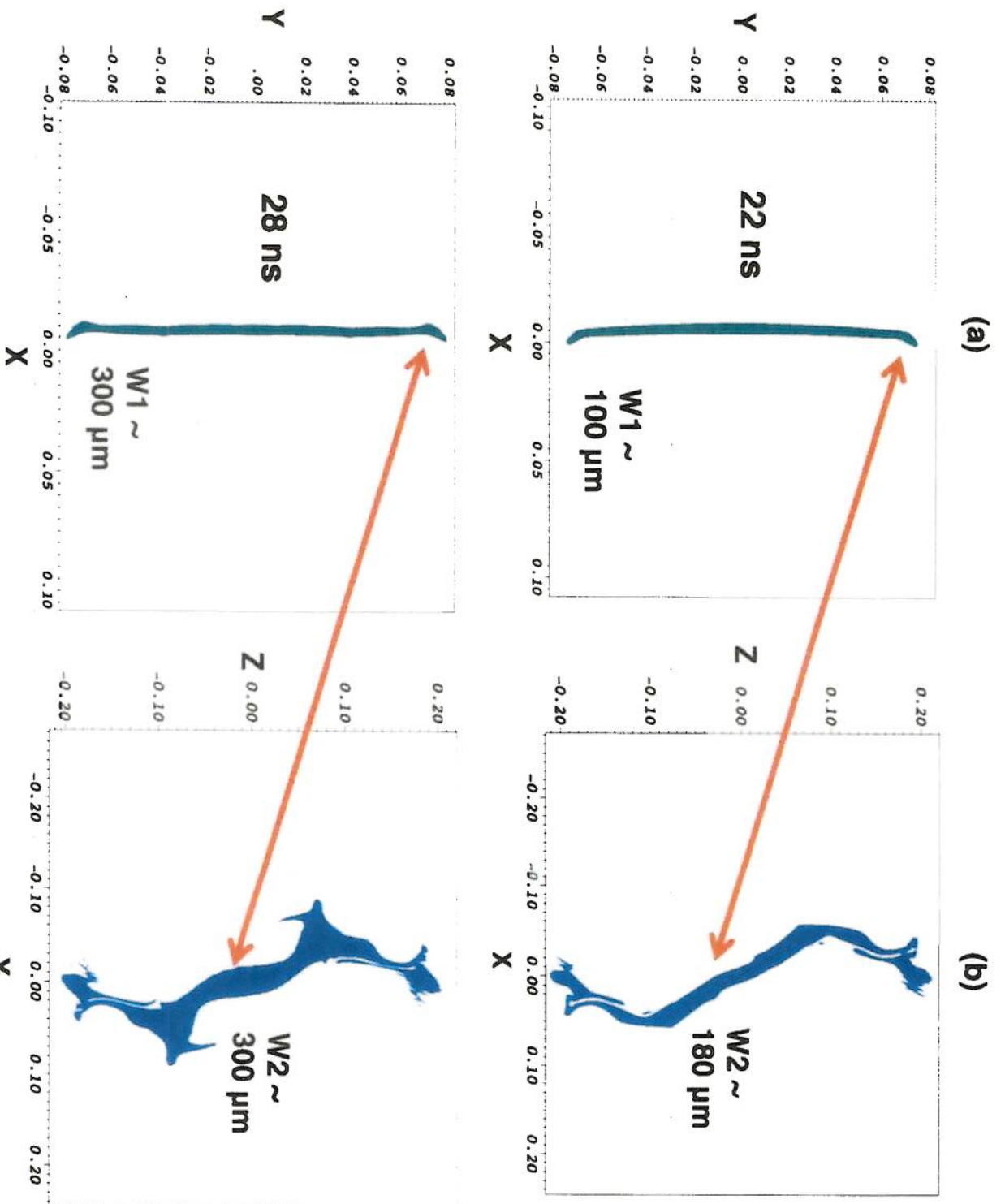


Fig. A3

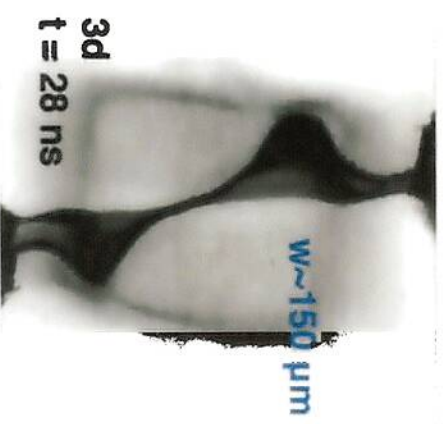
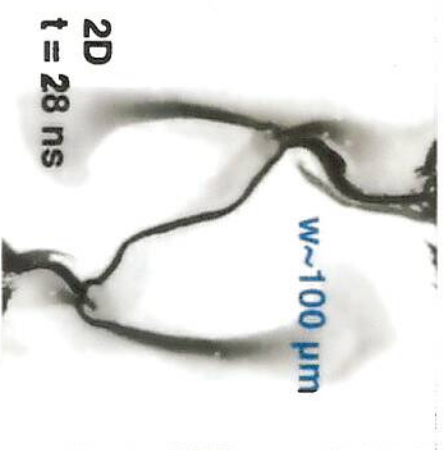


Fig. A4

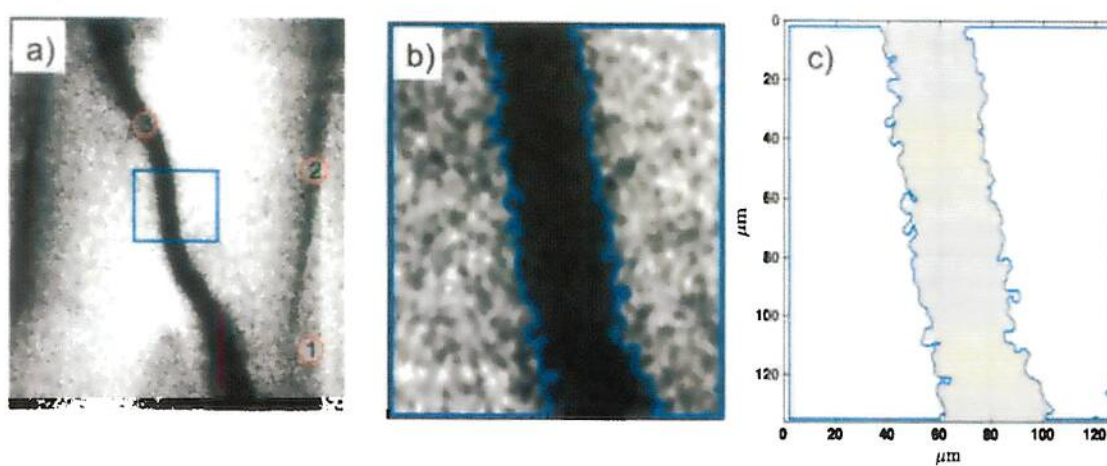


Fig. B1